The Astrophysical Journal, 639:788–802, 2006 March 10
© 2006. The American Astronomical Society. All rights reserved. Printed in U.S.A.

COMPACT H II REGIONS: WHAT LIES WITHIN?

Michael A. Dopita, Jörg Fischera, Oliver Crowley, and Ralph S. Sutherland
Research School of Astronomy and Astrophysics, Australian National University, Cotter Road, Weston Creek, ACT 2611, Australia; Michael.Dopita@anu.edu.au

Jessie Christiansen
School of Physics, University of New South Wales, Kensington, NSW 2052, Australia

Richard J. Tuffs and Cristina C. Popescu
Max-Plank-Institut für Kernphysik, Saupfercheckweg 1, 69117 Heidelberg, Germany

Brent A. Groves
Max-Planck-Institut fur Astrophysik, Karl-Schwarzchildstrasse 1, 85741 Garching, Germany

and

Lisa J. Kewley
Institute for Astronomy, 2680 Woodlawn Drive, Honolulu, HI 96822
Received 2005 February 9; accepted 2005 November 9

ABSTRACT

This paper presents both stellar mass and H II region diagnostics based on dusty, radiation-pressure-dominated photoionization models for compact and ultracompact H II regions, and compares these with observational constraints. These models successfully reproduce the observed relationship between the density and the thickness of the ionized layer. The absorption of ionizing photons in the dusty ionized plasma makes denser ionized regions thinner than simple photoionization models would predict, improving the fit with the observations. The models provide a good fit to observed diagnostic plots involving ratios of infrared emission lines, all accessible with the IRS instrument of the *Spitzer Space Telescope*. These give the effective temperature to an accuracy of about 2500 K and the mass of the ionizing star to a precision of about ±30%. The S IV/S III ratio is sensitive to foreground extinction as well as to stellar effective temperature or mass. From this ratio, we determine that the mean extinction to observed compact H II regions is typically $A_V \sim 30$ mag. The electron temperature depends on the chemical abundances, the pressure, and the effective temperature of the exciting star. We use these models to rederive the slope of the Galactic abundance gradient, with the result that $d\log(\mathrm{O/H})/dR_G = 0.06 \pm 0.01$ dex kpc^{-1}, bringing the Galactic abundance gradient derived from compact H II regions into closer agreement with those based on other techniques. The shape of the far-IR SED of compact H II regions can be used to constrain the mean pressure or density in the H II region. The *Spitzer* MIPS instrument should be very helpful in this regard.

Subject headings: circumstellar matter — dust, extinction — galaxies: starburst — H II regions — infrared: ISM — techniques: spectroscopic

Online material: color figure, machine-readable tables

1. INTRODUCTION

The compact and the ultracompact (UC) H II regions provide the first glimpse of the birth of massive stars, still embedded in their placental clouds of molecules and dust. Because of the extreme extinction in these clouds, these objects are only observable at radio, submillimeter, and infrared wavelengths. Nonetheless, they are of high intrinsic interest. They help us to understand the processes of massive star formation, study the initial mass function of massive stars, and may well be an important contributor to the spectral energy distribution (SED) of starburst galaxies (Rigby & Rieke 2004; Dopita et al. 2005). The whole field of both the observations of UC H II regions and current problems in understanding this class of objects has been recently reviewed by Churchwell (2002).

In this paper, the key parameter that we would like to derive from the observations of UC H II regions is the stellar mass (or, equivalently, the effective temperature) of the central star. As long as quantitative observations of this class of objects were limited to radio wavelengths, all we could do was to count the number of ionizing photons from the free-free radio continuum or from radio recombination lines and so infer the luminosity of the central star or stars. This entrains several difficulties. First, the theoretical number of ionizing photons emitted by the central star and the shape of the ionizing spectrum has been shown to be highly dependent on the atmospheric model used (Morisset et al. 2004). Second, if accretion onto the central star is still ongoing, the H II region may be "quenched" by the infalling matter (Walmsley 1995). Third, the dust within the H II region may very successfully compete to absorb the Lyman continuum photons, resulting in a smaller H II region and perhaps causing the mass of the central star to be subsequently underestimated.

This important effect of dust absorption has long been known and understood. First seriously quantified by Petrosian et al. (1972), it has been discussed by a number of authors since (Panagia 1974; Mezger et al. 1974; Natta & Panagia 1976; Sarazin 1977; Smith et al. 1978; Shields & Kennicutt 1995; Bottorff et al. 1998). More recently, its effect has been investigated and quantified (as far as possible by direct observation) in a series of papers by Inoue and his collaborators (Inoue et al. 2000, 2001; Inoue 2001). More

recently yet, Dopita et al. (2003) calibrated these correction factors using theoretical models of dusty H II regions, and Arthur et al. (2004) have specifically considered this effect in the context of photoionization models of compact and UC H II regions.

The *Infrared Space Observatory* (*ISO*) ushered in the era of quantitative IR spectroscopy of compact H II regions (Peeters et al. 2002; Martín-Hernández et al. 2002). Below 25 μm we see strong lines of [Ar II] 6.99 μm, [Ar III] 8.99 μm, [S IV] 10.51 μm, [Ne II] 12.81 μm, [Ne III] 15.55 μm, [S III] 18.71 μm, and [Ar III] 21.83 μm, while at longer wavelengths lines of [O III] 51.81, 88.36 μm, [O I] 63.18 μm, [N III] 57.34 μm, and [N II] 121.76 μm are all readily observable. These can be used to derive estimates of the electron density (Martín-Hernández et al. 2002). Furthermore, because lines of same atomic species are seen in multiple stages of ionization, we can construct line ratio diagnostics sensitive to the hardness (effective temperature) of the photoionizing source. These can then be used, in principle, to derive the stellar mass. Again, such diagnostics are subject to the limitations of the stellar atmospheric models adopted (Morisset et al. 2004).

In addition to the line diagnostics, the IR spectra contain strong molecular PAH features, infrared thermal emission by dust, and silicate absorption features, which can all be used to constrain the nature and geometry of the central H II region and the optical depth in the surrounding molecular cloud.

The *ISO* data set was quite limited, and there were a number of (sometimes severe) calibration problems to overcome, related to the very different apertures of the various spectroscopic modes. However, with the astounding success of the *Spitzer Space Telescope*, we now have the means to observe many more UC H II regions and to do so with much higher spectrophotometric accuracy. This paper aims to provide the observer with simple tools to interpret such observations and, specifically, to derive the mass or effective temperature of the central stars of UC H II regions.

2. THE PHOTOIONIZATION MODELS

The H II models presented here are all spherically symmetric, static, radiation-pressure-dominated, dusty photoionization models computed using the code MAPPINGS IIIr. These models are similar to those by Groves et al. (2004a, 2004b), which were used to model the spectra of the narrow-line regions of active galaxies. The dust grain model and the physical assumptions, such as PAH survival criteria and dust grain heating, contained in these models are essentially the same as those described in Dopita et al. (2005), and we refer the interested reader to that paper for details. Here we discuss only those aspects specific to the models presented in this paper.

2.1. *Stellar Atmospheres*

The situation as regards models of both the total production of ionizing UV photons and the shape of the photoionizing spectrum is remarkably unsatisfactory, as has been recently emphasized by Morisset et al. (2004). At some wavelengths, different atmospheric models may differ by factors of as much as 100 (or more) in their predictions of the ionizing flux! In principle, a self-consistent dynamical stellar atmosphere model, such as the CoStar models (Shaerer & de Koter 1997), should provide a more reliable spectrum. In practice, however, this is not the case. When compared with the observational constraints provided by photoionization modelling, the SED delivered by these models in the EUV is systematically too hard. In particular, these models show a strong excess flux at energies above the He II ionization edge. This has been noted and discussed several times in the literature (Crowther et al. 1999; Oey et al. 2000; Smith et al. 2002; Lumsden et al. 2003; Morisset et al. 2004). In her unpublished honors thesis, Christiansen (2003) found that these problems were acute in attempts to model UC H II regions. Crowther et al. (1999) found in their analysis of the stellar wind modelling in the CoStar models that this arises from an incomplete and approximate treatment of line blanketing, especially below the Lyman limit. This inevitably results in an overestimation of the ionizing photon flux and explains the spectral hardness of these models.

At the other extreme are found the "classical" Kurucz plane-parallel LTE line-blanketed models (Kurucz 1991, 1994), which display the softest EUV spectra and the lowest photoionizing flux. However, these models are restricted to $\log g = 3.0$ for the models with higher effective temperature, $T_{\rm eff}$. They therefore are more appropriate to dwarf stars than to the supergiants found in UC H II regions.

In between these extremes are found three sets of models with fairly similar photoionizing flux predictions (Morisset et al. 2004): the TLUSTY models of Lanz & Hubeny (2003), the WM-BASIC models of Pauldrach et al. (2001), and the CMFGEN models of Hillier & Miller (1998). Of these, the TLUSTY models are plane-parallel hydrostatic, while the other two model spherical dynamic atmospheres.

In this paper, we have elected to use the TLUSTY models, which have the advantage that the computed grid covers a very large range of $T_{\rm eff}$, $\log g$, and metallicity, as well as including over 100,000 individual atomic levels. The individual models in the grid[1] were interpolated and rebinned to the energy bins used in our photoionizing code, MAPPINGS IIIr. On the basis of the results presented by Morisset et al. (2004), we can expect that the diagnostics we derive here are very similar to those derived using either the WM-BASIC or the CMFGEN models.

Since the TLUSTY atmospheres have to be scaled to match the stellar dimensions, it is important to specify how this scaling is done. We have adopted the parameters of zero-age main-sequence (ZAMS) stars as computed by the Geneva group (Charbonnel et al. 1993; Maeder & Meynet 1988, 1989, 1994) and utilized by many of them in the CoStar models (Schaerer et al. 1993a, 1993b; Schaller et al. 1992). These are summarized in Table 1. Our photoionization models cover only the mass range 16.7–106.9 $M_{\odot}$, corresponding to an effective temperature ($T_{\rm eff}$) range 32,500–52,500 K. Our models also cover the cases of 0.5, 1.0, and 2.0 times solar metallicity to cover a range similar to that observed in Galactic UC H II regions (see Afflerbach et al. 1996; Martín-Hernández et al. 2002).

2.2. *Details of the Models*

In order to match within the H II region the chemical abundance set used in the TLUSTY "solar" abundance model atmospheres, we have adopted the Grevesse & Sauval (1998) abundance set, although we note that work by Asplund and his collaborators (Allende Prieto et al. 2001, 2002; Asplund 2000; Asplund et al. 2000) has recently revised the solar abundance calibration downward by nearly a factor of 2.

Since, in compact H II regions, the star has been formed out of portions of the cloud of interstellar material that now surrounds it, we have assumed that the chemical abundances of the star are identical to the abundance of the nebula that surrounds it. However, the gas-phase abundances in the nebula are lower than the total abundance because of the depletion of the heavy elements onto dust. The depletion factors are similar to the solar vicinity

[1] Available at http://tlusty.gsfc.nasa.gov.

TABLE 1
Stellar Parameters Used in the Models

$T_{\rm eff}$	$M/M_\odot$	$R/R_\odot$	log (g)	log ($L/L_\odot$)
30,000.....	13.86	4.677	4.240	4.200
32,500.....	16.7	5.20	4.230	4.431
35,000.....	20.0	5.77	4.217	4.650
37,500.....	23.6	6.41	4.207	4.862
40,000.....	29.8	7.23	4.196	5.076
42,500.....	36.4	8.09	4.184	5.279
45,000.....	44.9	9.03	4.179	5.475
47,500.....	55.8	10.05	4.179	5.662
50,000.....	77.8	12.16	4.152	5.917
52,500.....	106.9	14.71	4.132	6.166

values used by Dopita et al. (2005), based on the work by Jenkins et al. (1983) and Savage & Sembach (1996), but they have been supplemented, where possible, by the newer estimates of Kimura et al. (2003). These depletion factors are held constant as the abundance is increased or decreased. The dust-to-gas ratio is therefore proportional to the heavy-element abundance.

The effect on the star of increasing the abundance is to change both the number of ionizing photons that emerge from its atmosphere and to alter the shape of the ionizing spectrum. The main effect on the nebula is to decrease the electron temperature throughout the model and to increase the fraction of the ionizing photons absorbed by dust.

All models include dust absorption, photoelectric charging, heating, and the stochastic temperature fluctuations of dust grains. They also include radiation pressure acting on the charged grains and, through these, on the nebular gas as a whole. The dust model has been fully described in Dopita et al. (2005).

The photoionization models are characterized by the gas pressure, P, at the ionization front, taken here to be the point at which the fractional ionization of hydrogen falls to 0.5. The inner boundary of the models is taken to be located at 10% of the Strömgren radius computed for the initial pressure, P_i, chosen to give the desired outer pressure. The Strömgren radius has its usual definition, $R_s = (3N_*/4\pi n_e n_{\rm H}\beta)^{1/3}$, where N_* is the number of ionizing photons emitted by the star per second and n_e and $n_{\rm H}$ are the electron and hydrogen density at the inner boundary, respectively. The value β is the recombination coefficient of hydrogen at 10,000 K. The models cover the range in pressure $5.0 \leq \log P/k \leq 9.0$ cm^{-3} K.

In these static radiation-pressure-dominated dusty models, the gradient in the radiation pressure must match the gas pressure gradient, and consequently the local density in the ionized plasma increases strongly with radius in the nebula. This causes the emission measure to peak strongly close to the outer boundary of the nebula and ensures that most of these models would give the appearance of a thin ionized shell of gas if they could be observed at sufficient resolution at radio frequencies.

The emission spectra of H II regions are known to depend on metallicity, the pressure in the ionized gas, the SED of the photoionizing spectrum, and the geometry of the ionized gas with respect to the ionizing source, summarized in the ionization parameter: $\mathcal{U} = N_*/4\pi r^2 n_{\rm H} c$ (see, for example, Kewley et al. 2001). In these models, higher pressure corresponds to a higher mean ionization parameter in the H II region. The average ionization parameter in the H II region depends on the relative absorption by the dust and so cannot be predicted a priori. The actual computed values of $\log \mathcal{U}$, the logarithm of the volume-averaged value of the ionization parameter within the ionized region of the nebula, are tabulated in Table 2. As expected, compared with normal H II regions, these values are very high. For values of $\log \mathcal{U} > -2$, not only does the radiation pressure dominate the density structure, but the dust in the H II region also absorbs the majority of the ionizing photons (Dopita et al. 2002, 2003; see also Arthur et al. 2004). This condition is met for the majority of the models. Indeed, for the highest stellar masses and pressures, dust can absorb as much as 90% of the ionizing photons. The run of temperature and density with radius in one of these models is shown in Figure 1.

In order to compute the SED in the IR, including both the reemission spectrum from heated dust and the PAH molecular component, it is necessary to continue the models into the photodissociation region (PDR). We continue our pressure balance models until a column of $\log N_{\rm H} = 22.0$ is reached. This corresponds to an optical depth of several, as far as the far-UV photons are concerned. In this condition, the far-UV photons have effectively all been converted to photons in the far-IR dust reemission peak or into the PAH molecular emission bands.

Many UC H II regions are known to suffer visual extinction as high as 100 mag due to the extensive dust envelopes that surround them. These shells entirely remove the optical photons, give rise to prominent silicate and H_2O absorption features, and provide an additional cool-dust contribution to the SED in the 100–1000 μm wave band. These contributions are not computed here, but will be in a future paper. The far-IR SEDs presented here should therefore be regarded as the "intrinsic" SED of the UC H II region, which may well turn out to be somewhat different from the SED as actually observed through the dusty envelope. In order to facilitate the fitting of *Spitzer* IRS spectra of UC H II regions, in the Appendix we give the theoretical extinction curve

TABLE 2
Log of the Average Ionization Parameters in Solar Metallicity Models

	log (P/k)								
$M/M_\odot$	5.0	5.5	6.0	6.5	7.0	7.5	8.0	8.5	9.0
16.7.....	−3.43	−3.20	−2.97	−2.79	−2.62	−2.51	−2.39	−2.31	−2.23
20.0.....	−3.19	−2.97	−2.76	−2.60	−2.44	−2.32	−2.21	−2.14	−2.06
23.6.....	−3.02	−2.82	−2.62	−2.46	−2.31	−2.20	−2.10	−2.02	−1.95
29.8.....	−2.90	−2.70	−2.51	−2.37	−2.22	−2.11	−2.01	−1.94	−1.87
36.4.....	−2.79	−2.61	−2.43	−2.29	−2.15	−2.05	−1.95	−1.88	−1.81
44.9.....	−2.70	−2.50	−2.35	−2.21	−2.08	−1.98	−1.89	−1.82	−1.76
55.8.....	−2.62	−2.45	−2.28	−2.15	−2.02	−1.93	−1.84	−1.78	−1.72
77.8.....	−2.53	−2.36	−2.20	−2.08	−1.96	−1.87	−1.78	−1.74	−1.68
106.9.....	−2.44	−2.27	−2.13	−2.02	−1.91	−1.82	−1.74	−1.71	−1.65

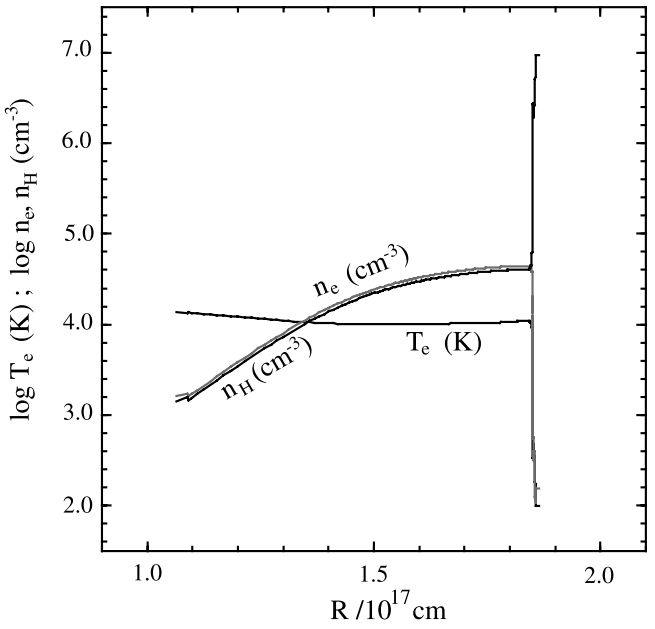

FIG. 1.—Temperature and density structure of a model having a central star of mass 45 $M_\odot$ and $P_i/k = 10^9$ cm^3 K at the ionization front. Note the strong increase in density resulting from the condition that the radiation pressure gradient matches the gas pressure gradient. [*See the electronic edition of the Journal for a color version of this figure.*]

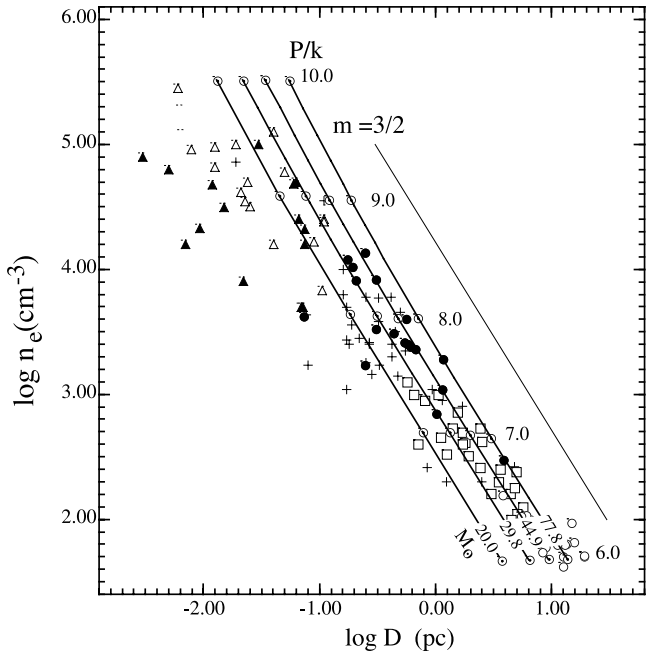

FIG. 2.—Diameter-density relationship for compact and UC H II regions. The observational points are from the compilation of data by Kim & Koo (2001), with the symbols having the same meaning as in Fig. 9. The points from Martín-Hernández et al. (2002) have been added as filled circles. The theoretical models for different stellar masses and initial pressures have been added as solid lines, and a line of slope 3/2 is shown for comparison. At high pressures, the slope of the theoretical curves is even steeper than 3/2 because the radiation pressure compresses the ionized gas into a thin layer close to the ionization front, leaving most of the volume with low emission measure.

for a best-fit dust mixture for the local interstellar medium. The details of the fitting process will be described elsewhere.

3. THE DENSITY-RADIUS RELATIONSHIP

Since each H II region is supported by the ionizations produced by the central star and the number of recombinations matches the number of ionizations, the extent of each H II region should be equivalent to a Strömgren radius. The expected relationship between the diameter, D, and the electron density, n_e, would then be $n_e \propto D^{-3/2}$. However, observations tell a different story. The compilation of data by Kim & Koo (2001) shows that the mean relation is best fit by a relation of the form $n_e \propto D^{-0.99\pm0.03}$. The data points used by Kim & Koo (2001) are reproduced in Figure 2. Here the sources of the data and the data point symbols are the same as in the Kim & Koo paper.

The deviation between the observed and expected slope of these relations has been subject to a number of different interpretations. Garay & Lizano (1999) argue that the more compact H II regions are excited by less massive stars, because they find a relationship between the number of ionizing photons inferred from the radio continuum flux and the diameter. However, the equation for the Strömgren radius gives $n_e \propto N_*^{1/2} D^{-3/2}$, which, when combined with the observational size-density relationship, $n_e \propto D^{-1}$, would imply $N_* \propto D$. The Garay & Lizano (1999) relationship has, rather, a slope of $N_* \propto D^2$, which does not resolve the problem. It should also be noted that errors in estimating the distance to individual objects will scatter data points in a luminosity-size relationship along a line $N_* \propto D^2$. Another problem with the Garay & Lizano (1999) interpretation is that the IR luminosity of many UC H II regions is known to exceed the flux that is consistent with excitation by a single star having a luminosity sufficient to ionize the H II region (Kurtz et al. 1994; Churchwell 2002).

Errors in distance estimates also affect the placement of points on the size-density relationship, along a line $n_e \propto D^{-1/2}$. This problem is particularly severe for those objects lying inside the solar circle (Martín-Hernández et al. 2002). In Figure 2 we plot the points derived for the objects observed by *ISO* as filled circles. Where the distance is ambiguous, both values have been plotted. Note the two filled circles lying below the 20 $M_\odot$ theoretical curve. These are both for a single object having a large distance ambiguity.

As pointed out by Kim & Koo (2001), the problem is further compounded by the fact that larger scale structures may remain undetected in interferometric radio observations, leading to a loss of flux and an underestimate of the true size. Their observations, as well as those by Martín-Hernández et al. (2003), show that such dense clumps are indeed surrounded by more extensive fainter structures and even provide evidence of multiple exciting sources.

Our models, as suggested by Martín-Hernández et al. (2003) and recently modelled by Arthur et al. (2004), provide yet another potential explanation for the flattening of the size-density relationship, namely, that dust absorbs a larger fraction of the ionizing photons in the smallest and densest H II regions. This is expected to reduce both the luminosity of the H II region and to make the effective thickness of the ionized layer thinner. The importance of dust absorption on the luminosity is a function of the metallicity, since the dust opacity scales with this quantity (Dopita et al. 2003).

The radio luminosities for our models can be computed from their absolute Hβ flux, converted using the formula for the ratio of the Hβ and radio flux density given in Dopita & Sutherland (2003):

$$F_{\mathrm{H}\beta}/S_{\nu_9} = 3.02\times10^{-10}\langle Z^2\rangle^{-1} Y^{-1} \nu_9^{0.1} T_4^{-0.51}, \qquad (1)$$

TABLE 3
PREDICTED INTEGRATED UC H II REGION FLUXES AT 5 GHz, log (Jy) AT A DISTANCE OF 1 kpc

$M/M_\odot$	$T_{\rm eff}/10^3$ K	log (P/k)								
		5.0	5.5	6.0	6.5	7.0	7.5	8.0	8.5	9.0
					0.5 $Z_\odot$					
16.7	32.5	0.396	0.388	0.376	0.357	0.334	0.306	0.275	0.243	0.210
20.0	35.0	0.871	0.858	0.838	0.813	0.781	0.743	0.705	0.660	0.620
23.6	37.5	1.239	1.221	1.197	1.165	1.126	1.081	1.035	0.987	0.944
29.8	40.0	1.554	1.512	1.503	1.467	1.424	1.373	1.323	1.273	1.226
36.4	42.5	1.818	1.793	1.760	1.720	1.673	1.620	1.566	1.513	1.466
44.9	45.0	2.055	2.027	1.990	1.947	1.896	1.841	1.784	1.728	1.680
55.8	47.5	2.270	2.239	2.200	2.153	2.099	2.042	1.981	1.927	1.878
77.8	50.0	2.542	2.504	2.460	2.408	2.351	2.292	2.231	2.177	2.131
106.9	52.5	2.794	2.754	2.707	2.650	2.591	2.529	2.471	2.419	2.377
					1.0 $Z_\odot$					
16.7	32.5	0.376	0.358	0.335	0.304	0.265	0.227	0.185	0.147	0.112
20.0	35.0	0.821	0.795	0.762	0.721	0.672	0.626	0.576	0.529	0.489
23.6	37.5	1.170	1.135	1.095	1.048	0.991	0.941	0.887	0.838	0.799
29.8	40.0	1.470	1.430	1.385	1.334	1.273	1.219	1.164	1.115	1.075
36.4	42.5	1.723	1.679	1.629	1.576	1.513	1.456	1.402	1.354	1.314
44.9	45.0	1.950	1.903	1.849	1.794	1.730	1.670	1.618	1.570	1.532
55.8	47.5	2.157	2.107	2.051	1.993	1.929	1.867	1.815	1.769	1.730
77.8	50.0	2.416	2.362	2.301	2.243	2.177	2.115	2.065	2.022	1.986
106.9	52.5	2.669	2.605	2.539	2.479	2.416	2.354	2.307	2.268	2.235
					2.0 $Z_\odot$					
16.7	32.5	0.314	0.280	0.271	0.236	0.188	0.143	0.100	0.062	0.028
20.0	35.0	0.713	0.684	0.653	0.614	0.560	0.507	0.458	0.413	0.375
23.6	37.5	1.027	0.990	0.954	0.916	0.859	0.803	0.751	0.706	0.670
29.8	40.0	1.303	1.259	1.221	1.187	1.129	1.072	1.021	0.978	0.945
36.4	42.5	1.540	1.496	1.452	1.423	1.364	1.307	1.258	1.217	1.185
44.9	45.0	1.756	1.710	1.664	1.638	1.580	1.524	1.476	1.437	1.406
55.8	47.5	1.955	1.907	1.860	1.836	1.778	1.724	1.677	1.639	1.608
77.8	50.0	2.204	2.155	2.106	2.085	2.029	1.976	1.932	1.898	1.869
106.9	52.5	2.444	2.394	2.346	2.325	2.268	2.220	2.179	2.147	2.121

where ν_9 is the frequency in gigahertz, Y is the number of electrons per hydrogen atom in the ionized gas, given to sufficient accuracy by

$$Y = 1 + \frac{N_{\rm He^+}}{N_{\rm H}} + \frac{N_{\rm He^{++}}}{N_{\rm H}}. \quad (2)$$

$\langle Z^2 \rangle$ is the mean charge per ion and T_4 is the mean electron temperature in the ionized gas in units of 10^4 K.

In Table 3 we list the predicted radio luminosities for our models in janskys at 5 GHz, reduced to a distance of 1.0 kpc. The effect of the dust absorption in the ionized plasma is evident from the reduction in the predicted flux with both metallicity and pressure in the model. For UC H II regions containing only a single star, this table can be used to infer the mass or effective temperature of the central star, provided that the distance of the object and the pressure or electron density have been determined. In cases in which the observed flux is greater than predicted from these models, the presence of multiple exciting stars can be inferred.

Because of the absorption by dust, the Strömgren column in our models shows less variation than might otherwise have been expected, a fact remarked on by Churchwell (2002) on the basis of observations, which are consistent with $\log N_{\rm H\,II} \sim 21.5$ for most objects. The computed Strömgren columns are given in Table 4. These Strömgren columns correspond to dust optical depths in the ionized plasma at visual wavelengths of order unity or even greater.

The theoretical density-radius relationship is shown as the curves in Figure 2. A line of slope 3/2, expected for simple Strömgren theory, is also plotted for comparison. At first sight, it is somewhat surprising that at high pressures, these theoretical curves display a slope even steeper than 3/2. However, this is explained as the result of the radiation pressure acting in the ionized plasma, which compresses the ionized gas into a thin layer close to the ionization front. Thus, most of the volume is filled with ionized gas at a much lower density, leading to the H II region having a greater diameter than would be expected from simple Strömgren theory.

Kim & Koo (2001) have noted that the radio observations are most likely to pick up on the high emission measure regions of the UC H II region. Therefore, a more appropriate measure of the characteristic dimension of the H II region might be the thickness of the ionized layer, which is the ratio of the Strömgren column given in Table 4 divided by the mean electron density. This quantity is plotted in Figure 3. Both the slope and the shape of the theoretical curves in this diagram are now in better agreement with the observations.

At low pressures, the curves in Figures 2 and 3 converge, as the effect of dust absorption and radiation pressure becomes

TABLE 4
COMPUTED CENTRAL STRÖMGREN COLUMNS OF MODELS log (N_H) cm^{-2}

		log (P/k)					
$M/M_\odot$	$T_{eff}/10^3$ K	5.0	6.0	7.0	8.0	9.0	10.0
			0.5 $Z_\odot$				
16.7	32.5	20.32	20.64	20.92	21.16	21.34	...
20.0	35.0	20.47	20.78	21.05	21.28	21.44	...
23.6	37.5	20.59	20.89	21.15	21.36	21.52	...
29.8	40.0	20.69	20.98	21.24	21.44	21.59	...
36.4	42.5	20.77	21.06	21.31	21.50	21.64	...
44.9	45.0	20.84	21.13	21.37	21.55	21.68	...
55.8	47.5	20.91	21.19	21.42	21.60	21.72	...
77.8	50.0	20.99	21.26	21.48	21.65	21.76	...
106.9	52.5	21.08	21.33	21.54	21.69	21.79	...
			1.0 $Z_\odot$				
16.7	32.5	20.32	20.62	20.87	21.06	21.20	21.29
20.0	35.0	20.46	20.75	20.99	21.16	21.29	21.37
23.6	37.5	20.57	20.85	21.08	21.24	21.36	21.43
29.8	40.0	20.67	20.94	21.16	21.31	21.42	21.48
36.4	42.5	20.76	21.01	21.22	21.36	21.46	21.53
44.9	45.0	20.82	21.07	21.27	21.40	21.49	21.55
55.8	47.5	20.88	21.12	21.31	21.44	21.52	21.59
77.8	50.0	20.96	21.19	21.36	21.48	21.55	21.62
106.9	52.5	21.01	21.24	21.41	21.52	21.58	21.64
			2.0 $Z_\odot$				
16.7	32.5	20.31	20.61	20.79	20.94	21.05	...
20.0	35.0	20.44	20.73	20.89	21.03	21.13	...
23.6	37.5	20.55	20.83	20.97	21.10	21.19	...
29.8	40.0	20.65	20.91	21.04	21.16	21.24	...
36.4	42.5	20.74	20.98	21.09	21.20	21.28	...
44.9	45.0	20.80	21.03	21.13	21.24	21.30	...
55.8	47.5	20.86	21.07	21.16	21.26	21.33	...
77.8	50.0	20.93	21.12	21.20	21.29	21.35	...
106.9	52.5	20.97	21.16	21.25	21.32	21.37	...

negligible. Figure 2 would imply that most of the exciting sources are single stars, since the upper envelope of the curves lies above the upper envelope of the observed points on the diagram. However, Figure 3 tells a different story, suggesting that multiple exciting sources may be common, as argued on the basis of morphology by Martín-Hernández et al. (2003). The most reliable indicator of multiplicity of exciting stars is to compare the absolute free-free radio luminosity with the figures given in Table 3.

The size measured at radio wavelengths will depend on the instrument used to observe it and is most likely to be intermediate between the limits of Figures 2 and 3. However, given that UC H II regions display a wide range of morphologies—shell, bipolar, cometary, core-halo, etc. (Wood & Churchwell 1989; Afflerbach et al. 1996; Kim & Koo 2001)—it is clear that the simple spherical models presented here are an oversimplification of reality and that dynamical modelling in the complex three-dimensional density structure in the surrounding interstellar medium is required for a full description and understanding of the density-radius relation.

We conclude that these radiation-pressure-dominated photoionization models can reasonably explain the form of the density-diameter relationship as a result of the absorption of the ionizing photons by the dust within the ionized regions of UC H II regions, but this relationship is not useful in constraining the mass of the central star or stars. The integrated radio continuum flux density should be used for this purpose.

The mean density in the H II region is very closely correlated with the pressure at the ionization front. For the objects for which *ISO* spectroscopy exists, these pressures can be read off either Figure 2 or 3 and lie in the range $7.0 \leq \log(P/k) \leq 8.6$ cm^{-3} K.

4. RECALIBRATION OF THE GALACTIC ABUNDANCE GRADIENT

As shown by Afflerbach et al. (1996), the measured electron temperature of UC H II regions, like those of more normal H II regions (Shaver et al. 1983), is a fairly strong function of Galactocentric radius. This has been correctly interpreted by both these authors as mainly the result of a Galactic abundance gradient. Higher metallicity puts more coolants into the ionized plasma, which results in a decrease in the equilibrium electron temperature. However, as was recognized by Afflerbach et al. (1996), the temperatures of H II regions also depend on the effective temperature of the exciting stars. Furthermore, for the UC H II regions, the electron temperatures depend on the electron density or pressure in the ionized gas. Collisional quenching of cooling lines leads to systematically higher electron temperatures in these objects. The quantification of each of these effects is given in Figure 4 for our grid of models.

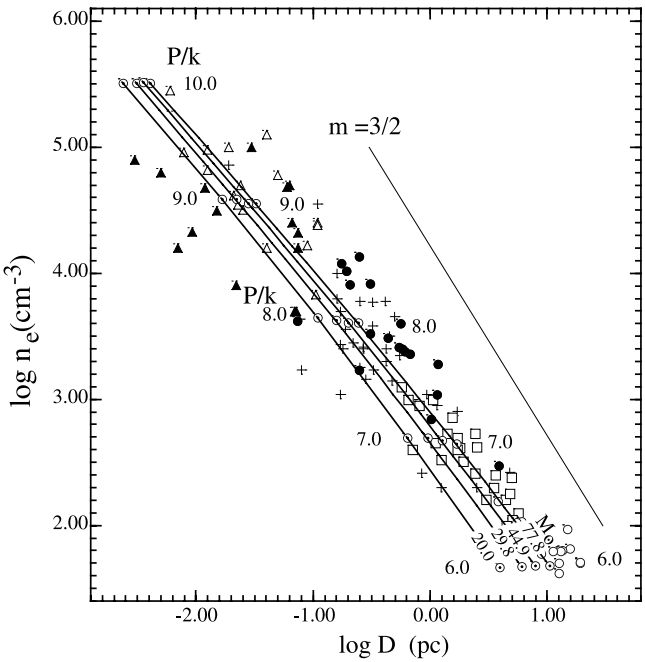

FIG. 3.—Same as Fig. 2, but with the curves plotting the computed thickness of the ionized layers in the models instead of the diameter of the physical diameter of the H II region. This quantity is smaller than the physical diameter because the radiation pressure confines the ionized layer into a thin shell. Because radio interferometers are most sensitive to the highest surface brightness features in an extended structure, this quantity may be a more appropriate measure in the interpretation of the radio observations, as noted by Kim & Koo (2001).

These new dusty, radiation-pressure-dominated models can now be used to recalibrate the slope of the Galactic abundance gradient determined by Afflerbach et al. (1996) by first solving for both the pressure and for the mass (or effective temperature) of the ionizing stars and then using these values to determine the value of the oxygen abundance in units of $12 + \log(\mathrm{O/H})$, which is consistent with the observed temperature. The result of this analysis is shown in Table 5. Pressures given in parentheses are estimates only. Masses are generally determined from the radio-integrated flux densities using Table 3. However, in some cases, identified in the table as, for example, 26(IR), they have been determined from the nebular excitation given from the *ISO* spectroscopy of Peeters et al. (2002). The method used is described in the following section. In the two cases in which both luminosity and excitation estimates can be made, they are in good agreement. In some objects the radio flux density is greater than is predicted by the models. These are probably excited by more than one star, and for these objects the mean central star mass of $\sim 40\ M_{\odot}$ is assumed.

Figure 5 shows the derived Galactic abundance gradient. The errors are those due the error in measuring the electron temperature. No error in determining R_G was given in the source paper. For clarity, objects at the same Galactocentric radius have been separated by 0.1 kpc in R_G on this plot. The estimated gradient of the Galactic oxygen abundance [$d \log(\mathrm{O/H})/dR_G = -0.06 \pm 0.01$ dex kpc^{-1}] is somewhat higher than that derived by Afflerbach et al. (1996) [$d \log(\mathrm{O/H})/dR_G = -0.047 \pm 0.009$ dex kpc^{-1}].

This recalibration brings the measured Galactic abundance gradient for UC H II regions into closer agreement with the other methods involving H II region observations. For example, Shaver et al. (1983) used a combination of recombination line temperatures and optical observations of H II regions to obtain a value

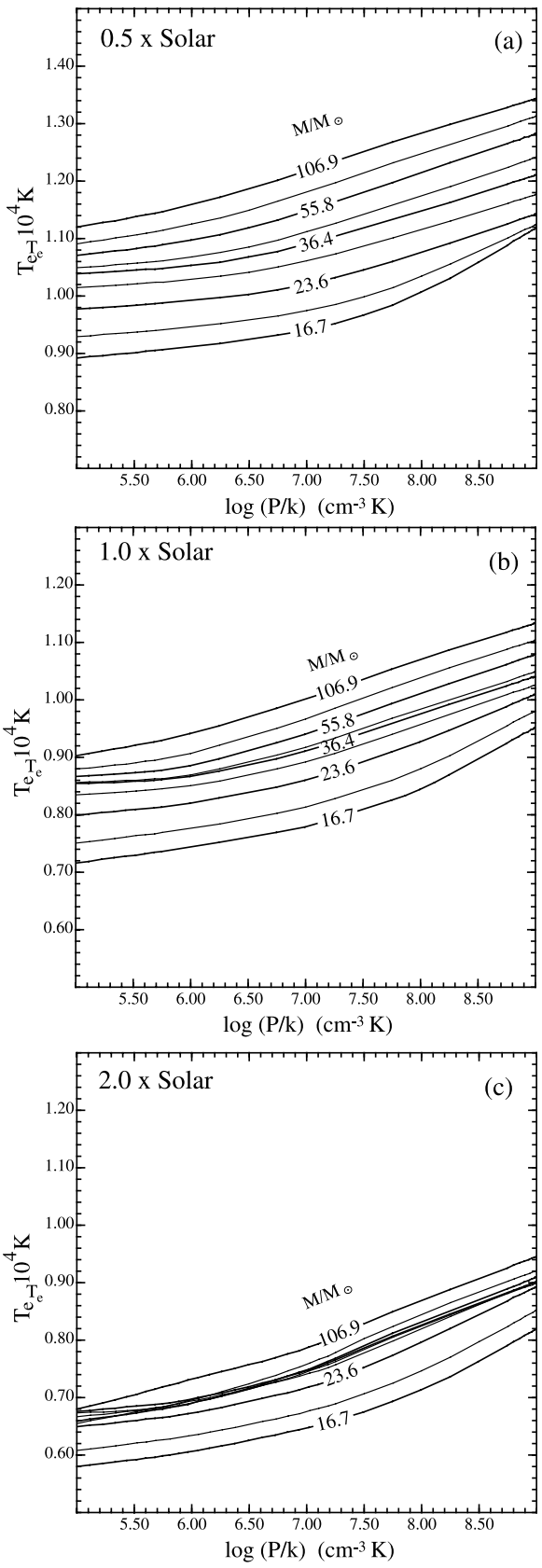

FIG. 4.—Mean electron temperature in the ionized plasma in our model grid is given as a function of pressure and stellar mass for (*top to bottom*) 0.5, 1.0, and 2.0 times the solar metallicity.

TABLE 5
COMPUTED CENTRAL STRÖMGREN COLUMNS OF MODELS $\log(N_H)$ cm^{-2}

Source	D_G (kpc)	log (P/k)	$M/M_\odot$	12 + log (O/H)
G5.89	6.0	8.3	45	$9.36^{+0.21}_{-0.21}$
G11.94	4.3	7.8	36	$9.25^{+0.08}_{-0.02}$
G25.40	4.1	7.6	(40)	$9.33^{+0.14}_{-0.17}$
G29.96	4.2	7.8	26(IR)	$9.47^{+0.05}_{-0.06}$
G32.80A	7.5	7.7	30(IR)	$9.31^{+0.15}_{-0.18}$
G32.80B	7.5	7.6	30(IR)	$9.08^{+0.19}_{-0.17}$
G37.87	5.8	7.9	(40)	$9.35^{+0.15}_{-0.26}$
G45.12	6.4	8.2	(40)	$9.16^{+0.10}_{-0.10}$
G45.45	6.2	7.7	106	$9.04^{+0.15}_{-0.21}$
G70.29	9.9	8.2	40(IR)	$9.12^{+0.14}_{-0.24}$
G70.33	9.9	7.8	78	$9.00^{+0.17}_{-0.22}$
G81.7B	8.6	8.0	30, 26(IR)	$9.14^{+0.14}_{-0.21}$
G81.7C	8.6	8.2	40	$9.10^{+0.13}_{-0.34}$
G81.7D	8.6	8.1	22	$9.09^{+0.16}_{-0.28}$
G111.54	10.3	(8.0)	(40)	$9.00^{+0.08}_{-0.11}$
G133.7B	10.8	8.0	40, 40(IR)	$9.06^{+0.14}_{-0.27}$

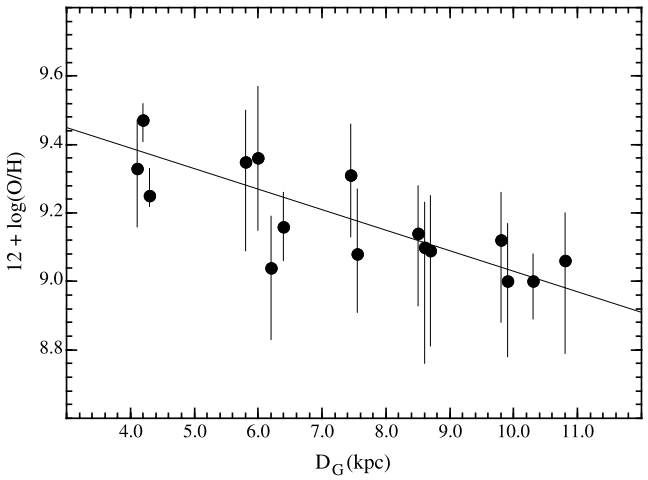

FIG. 5.—Galactic abundance gradient for UC H II regions according to our recalibration of the results of Afflerbach et al. (1996). The fitted slope is $d\log(O/H)/dR_G = 0.06 \pm 0.01$ dex kpc^{-1}.

of $d\log(O/H)/dR_G = -0.07 \pm 0.02$ dex kpc^{-1}; Simpson et al. (1995) used Kuiper Airborne Observatory observations of far-IR fine structure lines to find $d\log(O/H)/dR_G = -0.08 \pm 0.01$ dex kpc^{-1}; and Afflerbach et al. (1997) used the same technique to obtain $d\log(O/H)/dR_G = -0.064 \pm 0.009$ dex kpc^{-1}. More recently, Martín-Hernández et al. (2002) used the *ISO* spectroscopy of compact H II regions to determine the Galactic abundance gradient of element ratios and used the Galactic electron temperature gradient to estimate absolute abundance ratios of the α-process elements Ne and Ar: $d\log(Ne/H)/dR_G = -0.06$ dex kpc^{-1} and $d\log(O/H)/dR_G = -0.07$ dex kpc^{-1}. In a later paper Martín-Hernández et al. (2003), somewhat smaller gradients were found for these elements: $d\log(Ne/H)/dR_G = -0.039$ dex kpc^{-1} and $d\log(O/H)/dR_G = -0.056$ dex kpc^{-1}, respectively, but with large scatter on the observed points. The ensemble average of all of these techniques gives an (H II region determined) abundance gradient of $d\log(O/H)/dR_G = -0.068 \pm 0.007$ dex kpc^{-1}. It should be noted that this value is in good agreement with the results of non-LTE analysis of B-type stellar spectra: $d\log(O/H)/dR_G = -0.06 \pm 0.01$ dex kpc^{-1} (Smartt & Rolleston 1997).

5. EXCITATION PLOTS

The excitation sequences of compact and UC H II regions provide constraints on the form of the EUV spectrum and therefore on the effective temperature (and hence the mass) of the central star. The limitations of this technique have recently been fully analyzed by Morisset et al. (2004). These authors demonstrate that the results are highly dependent on the choice of model atmospheres, since this choice fixes the number of ionizing photons in the band of energies sufficient to ionize whatever ionic species is being considered. Thus, the results of this section are stellar atmospheric model dependent. As has already been explained, our results with the TLUSTY model atmospheres should be quite similar to those that would be obtained with the WM-BASIC or CMFGEN stellar atmosphere models, but the CoStar models would give a higher degree of excitation at a given mass.

In Figure 6 we plot the [Ne III] 15.5 μm/[Ne II] 12.8 μm ratio versus the [S IV] 10.5 μm/[S III] 18.7 μm ratio as a function of both the mass of the central star (i.e., effective temperature and initial pressure in models having solar and twice solar metallicity). The systematic variation of the [S IV] 10.5 μm/[S III] 18.7 μm ratio as a function of pressure is due to the lower critical density for deexcitation of the [S III] 18.7 μm line as compared with the [S IV] 10.5 μm ($\sim 2\times10^4$ cm^{-3} as compared with $\sim 6\times10^4$ cm^{-3}), as well as the fact that, in these radiation-pressure-dominated models, the [S III] line is formed in a region of intrinsically higher density than the [S IV] line.

Note that these line ratios are both rather insensitive to metallicity; a factor of 2 change in metallicity will change the estimate of effective temperature by about 2500 K, corresponding to a change in mass of about 20%. We note that the sensitivity of the mass estimate to chemical abundances is less than that found by Morisset (2004) using the WM-BASIC stellar models. However, the stellar model atmospheres adopted, the modelling code used, and the structure of the H II region models are all different, and it is not clear to us which of these differences is the main explanation for the different sensitivity of the computed line ratios to abundance.

For UC H II regions excited by more than one star, this excitation diagram, as well as the others presented below, should be thought of as indicating the probable mass of the most massive exciting source, since this is the star that will dominate the flux of UV photons.

Although the slope of the theoretical curves in Figure 6 agrees with the observations, the curves in the correct range of pressures, $6 \leq \log(P/k) \leq 8$, lie above the observed points by about 0.5 dex. It is possible that some of this discrepancy is model dependent, and part may be the result of uncertain aperture correction factors in the *ISO* observations. However, it is certain that most is due to reddening (since the line ratios uncorrected for reddening are presented here). This would lead to a diminution of the S IV] 10.5 μm/[S III] 18.7 μm ratio because the S IV] 10.5 μm line lies well within the 10 μm silicate absorption feature, which is often observed to be strong in these objects. Using our extinction curve, we have estimated the reddening vector corresponding to $A_V = 30$ mag. It is clear that a mean foreground extinction of this magnitude would bring the observations into accord with theory. This is of similar magnitude to that estimated by Martín-Hernández et al. (2002). They found that the differential reddening between the S IV] 10.5 μm line and the [S III] 18.7 μm line amounts to 0.212 mag per magnitude of extinction in the K wave band, which these authors infer to lie

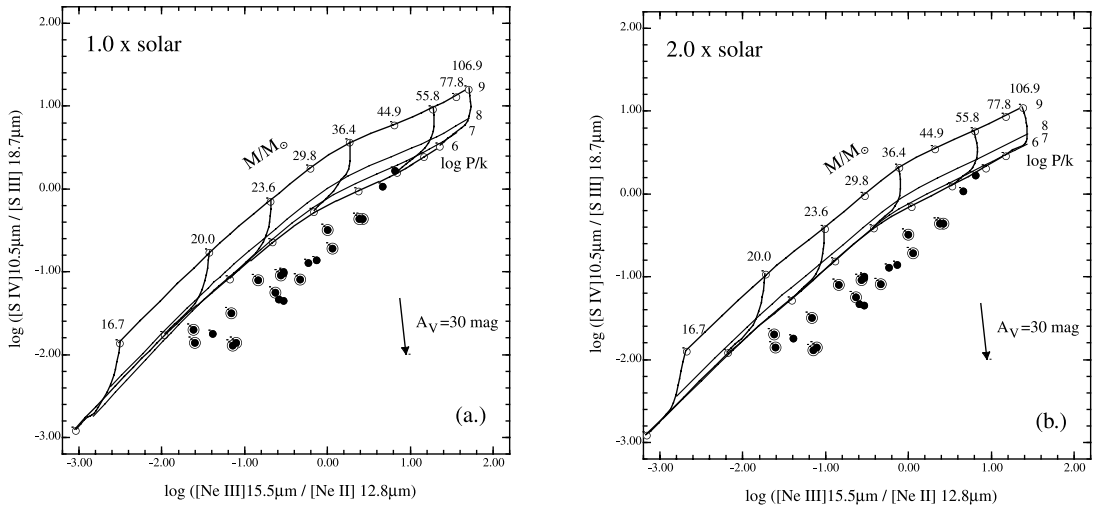

FIG. 6.—Theoretical [Ne III] 15.5 μm/[Ne II] 12.8 μm ratio vs. the [S IV] 10.5 μm/[S III] 18.7 μm ratio as a function of both mass of the central star and initial pressure in the model. The left panel corresponds to a metallicity of 1.0 times solar, and the right panel to 2.0 times solar. The plotted points are from Peeters et al. (2002) (*filled circles*). The subset of these data for which both radio diameter and density information is available from Martín-Hernández et al. (2002) are emphasized by the addition of a circle around the point. For observational errors, see those papers. Because [S IV] 10.5 μm lies in the silicate absorption feature, there is appreciable sensitivity to reddening. The reddening vector corresponding to $A_V = 30$ mag is indicated. If the mean foreground reddening of the observed UC H II regions were of this magnitude, then theory and observation would be brought into agreement.

anywhere between 0 and 2.7 mag using the H I recombination lines. Since we are looking for simple mass diagnostics for the exciting star, the sensitivity to foreground reddening of the [S IV] 10.5 μm/[S III] 18.7 μm ratio is something of an inconvenience.

These uncertainties may be eliminated by the substitution of the [Ar III] 9.0 μm line in place of the [S III] 18.7 μm line (see Fig. 7). Since the [Ar III] 9.0 μm line lies on the other side of the silicate absorption feature, it suffers from extinction very similar extinction to the [S IV] 10.5 μm feature. Indeed, Martín-Hernández et al. (2002) estimate these two lines have exactly the same total extinction. Furthermore, because the lines are so close together in wavelength, the aperture corrections and flux calibration errors will be almost identical. These advantages prevail over the disadvantage that they are lines of different elements, so their line ratios will depend on the relative abundances of the elements. This should not be a serious problem, since both are α-process elements, and so their relative abundances are not expected to vary appreciably.

The line ratios of Figure 7 show little sensitivity to pressure, and the theoretical curves are in close agreement with the observations. The points are consistent with central star masses from $\sim$20 $M_\odot$ up to about 55 $M_\odot$. The range of both ratios is large, so each provides good sensitivity when used as a mass diagnostic. The same is also true when the Ne III] 15.5 μm/[Ne II] 12.8 μm ratio is plotted versus the [Ne III] 15.5 μm/[S III] 18.7 μm ratio (Fig. 8).

Here, we have not plotted diagnostics involving the [Ar III] 9.0 μm/[Ar II] 7.0 μm ratio because the Ar II lines in the models are apparently much too weak. Because the absolute strength of the [Ar II] 7.0 μm is much larger in very low density models, we believe that the (magnetic dipole) transition probability for the [Ar II] 7.0 μm line used in MAPPINGS ($A_{ij} = 0.0562$ s^{-1}), as

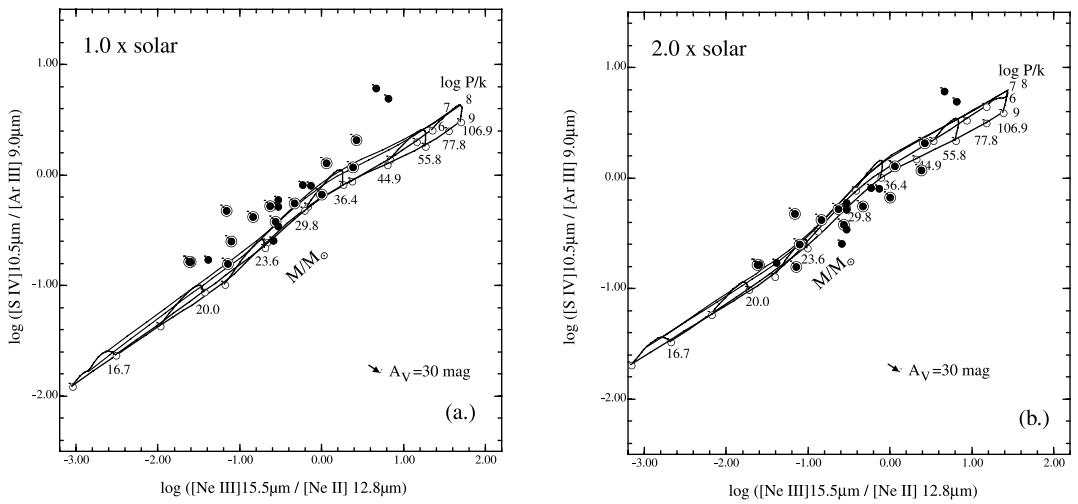

FIG. 7.—Same as Fig. 6, but for the [Ne III] 15.5 μm/[Ne II] 12.8 μm ratio vs. the [S IV] 10.5 μm/[Ar III] 9.0 μm ratio. Use of these ratios eliminates sensitivity to foreground extinction. The models and observations are in very good agreement for the range of pressures and abundances inferred for these objects. In combination with Fig. 6, this figure allows the determination of $T_{\rm eff}$ (or mass) of the exciting stars and the foreground reddening.

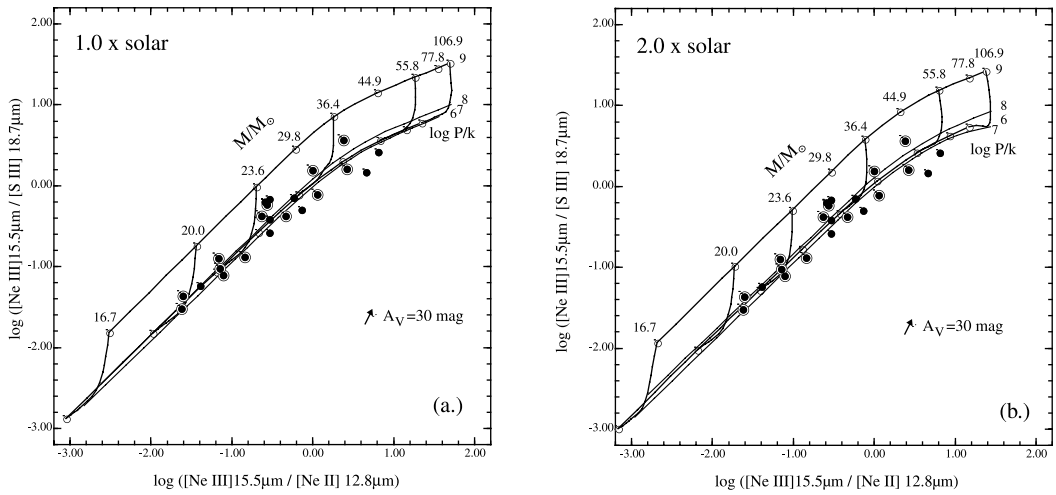

FIG. 8.—Same as Fig. 6, but for the [Ne III] 15.5 μm/[Ne II] 12.8 μm ratio vs. the [Ne III] 15. 5μm/[S III] 18.7 μm ratio.

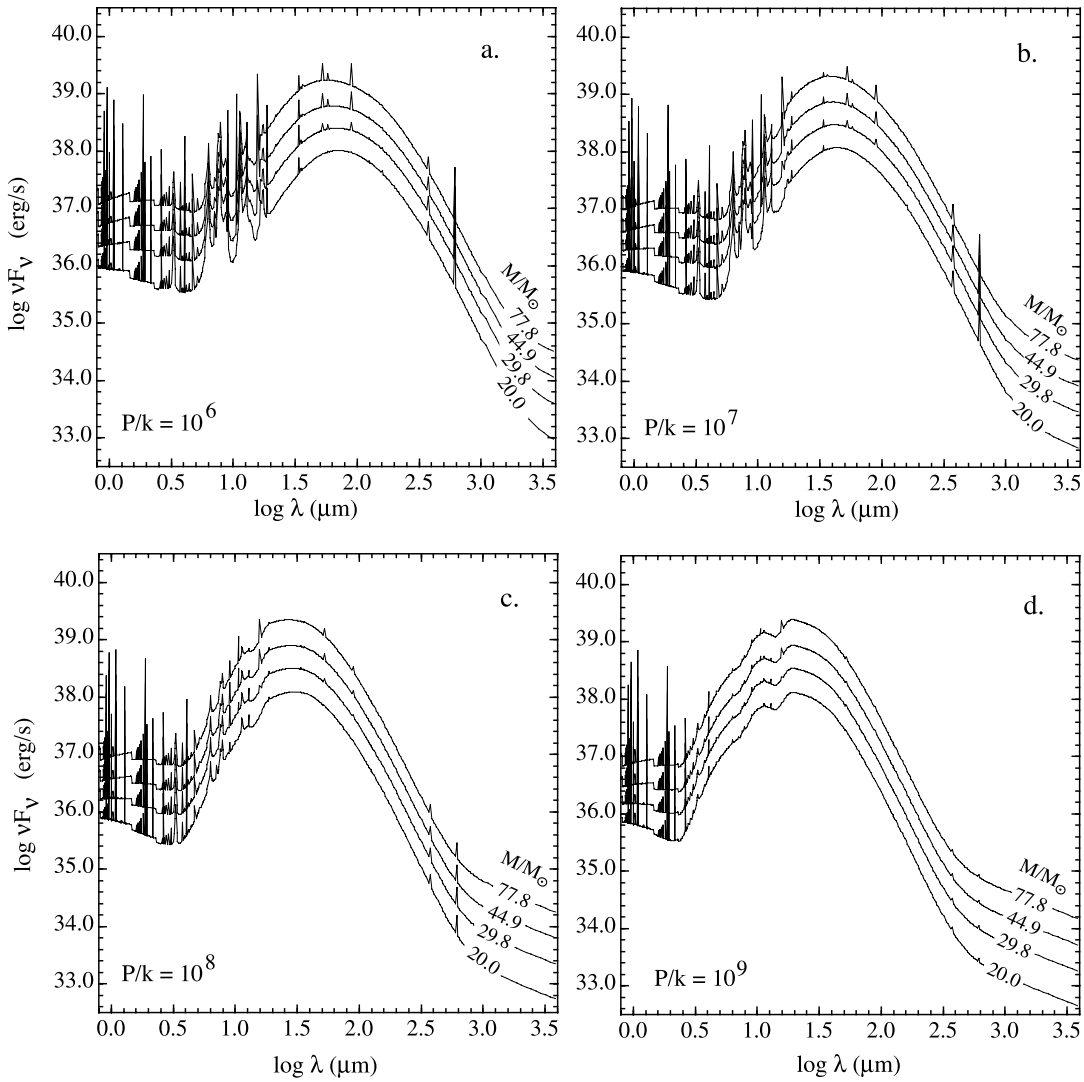

FIG. 9.—Variety of SEDs generated in these models. For clarity, only four stellar masses are plotted for each pressure, as follows: $P/k = 10^6$ cm^{-3} K (*a*); $P/k = 10^7$ cm^{-3} K (*b*); $P/k = 10^8$ cm^{-3} K (*c*); and $P/k = 10^9$ cm^{-3} K (*d*). Note that as the pressure increases, the far-IR peak shifts to shorter wavelengths because the H II regions become more compact. At the same time, every emission line as well as the free-free nebular continuum above 1000 μm becomes weaker with respect to the dust continuum, as dust absorbs relatively a greater fraction of the ionizing photons. Moreover, the PAH features weaken with respect to the thermal far-IR dust reemission as more of the radiation field is absorbed in the ionized plasma. At high pressures the silicate 10 and 20 μm bands appear in emission.

well as in other codes, and which was taken from Mendoza (1983), is almost certainly in error. The published transition probability appears to have its origin in the thesis of Naqvi (1952) and is apparently too low, leading to too much collisional quenching of this line at the high pressures inferred in this paper. This transition probability should be recomputed.

A similar problem with the [Ar II] 7.0 μm line intensity has also been noted by Morisset et al. (2004), who prefers to ascribe it to our inadequate knowledge of the dielectronic recombination coefficients of Ar III. The recombination rate would have to be increased by a factor of on the order of 10 to make model and observation agree. Both explanations for the weakness of the [Ar II] 7.0 μm line in models are plausible, and both emphasize the need for more theoretical work to be done on the Ar ions.

In conclusion, we have found that four line ratios, all readily measured with the *Spitzer* IRS instrument Houck et al. (2004), should provide fairly reliable mass (or $T_{\rm eff}$) estimates for the central star. As shown in the previous section, in the few cases where both have been estimated, the masses estimated from nebular excitation are in good agreement with masses derived from the absolute luminosities of their H II regions.

6. IR SPECTRAL ENERGY DISTRIBUTIONS

The variety of SEDs given by these models is presented in Figure 9. These SEDs are available in electronic form in the online version of this paper (see the Appendix). As emphasized above, these SEDs are the "source function" SEDs of H II regions, including the thin compressed H I shell around these, to a total H I column density of $\log N_{\rm H} = 22.0$. As such, they cannot display the absorption of the overlying cold molecular gas, or the ices associated with it. To produce the emergent SED of both the H II region and its shell of cold gas requires a further radiation transfer computation, which, since it needs to account for the scattered light, has to be fully three-dimensional. Such models will be described in a separate paper.

The SEDs in Figure 9 differ widely from each other, depending on the compactness of the H II region, on which pressure parameter we have used, and to a lesser extent on the mass of the central star. In general, more luminous and more compact H II regions have hotter dust. At the highest pressures, the dust reemission continuum comes to dominate the total continuum down to below 1 μm. Apart from this (physically obvious) distinction, there are more subtle effects on the SED visible in Figure 9.

First, as the pressure increases, the emission lines become weaker with respect to the dust continuum. This effect, explained in Dopita et al. (2002, 2003) is a result of the fraction of the ionizing photons absorbed by the dust being a direct function of the mean ionization parameter $\mathcal{U}$, and it amounts to more than 50% when $\log \mathcal{U} > -2$. As can be seen in Table 2, $\mathcal{U}$ increases strongly with both pressure and with stellar mass.

Second, and related to the first point, the continuum above 1000 μm drops systematically with increasing pressure. This continuum is principally the free-free emission from the nebula, so as pressure increases, dust absorbs more and more of the ionizing continuum, the H II region shrinks, and the free-free continuum becomes weaker with the lines. However, because the dust becomes hotter, the far-IR bump shifts to shorter wavelengths, and the wavelength region over which the free-free emission dominates becomes greater. For $P/k = 10^5$ cm^{-3} K, the free-free emission dominates at wavelengths greater than 3 mm, but for the $P/k = 10^8$ cm^{-3} K models, the free-free emission is the main source of continuum at any wavelength above 300 μm.

Third, the PAH continuum emission bands weaken with both increasing stellar mass and increasing pressure parameter. In our models, the PAH molecules are effectively destroyed by photodissociation wherever there are sufficient photons to doubly ionize the species. For coronene, this means that any photons above ~13.6 eV can photodissociate it. This effectively confines the PAH molecules to the PDR around the ionized H II region. This effect has been most clearly observed in the stunning images of the Galactic H II region RCW 49 by Whitney et al. (2004) and Churchwell et al. (2004), which shows strong PAH emission confined behind the (dust continuum emitting) complex of ionization fronts and "elephant trunk" features in this object. It has also been observed in compact H II regions by Burton et al. (2000). Mostly, the PAH bands are excited by the nonionizing UV photons that penetrate the PDR. As pressure in the H II region increases, the column density in the ionized plasma increases (see Table 4), and a greater fraction of both the ionizing and the nonionizing photons is absorbed within the H II region, leaving fewer to excite the PAH molecules within the PDR.

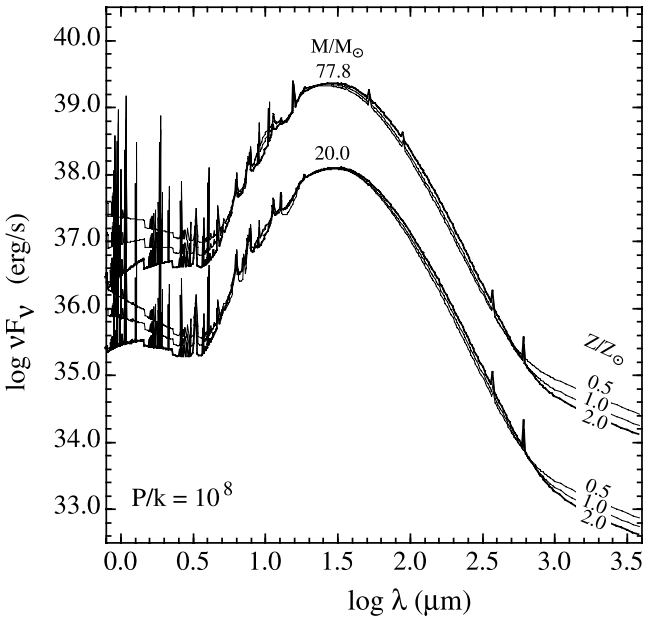

FIG. 10.—SEDs for two stellar masses (20 and 77.8 $M_\odot$) shown as a function of metallicity for a fixed pressure: $P/k = 10^8$ cm^{-3} K. Differences at the long wavelength end are due to differences in the ionized mass, mostly determined by the dust absorption in the ionized gas, and at the short wavelength, the differences can be ascribed to the different absorption produced by the (fixed) column density of the atomic hydrogen shell ($\log N_{\rm H\,I} \sim 22.0$) used in these models. In the far-IR dust peak itself, the differences induced by changing abundances are negligible.

Finally, because the dust in the H II region is hot, the silicate features at 10 and 20 μm appear in emission rather than absorption. At intermediate pressures, $P/k \sim 10^6$, the combination of these emission bands superimposed on the more general far-IR dust emission produces the appearance of an absorption feature, or "notch," at about 15 μm. This type of feature is observed in a number of the H II regions observed with *ISO* by Peeters et al. (2002), but most notably in IRAS 21190+5140 and IRAS 23030+5958.

The shape of the SED in the far-IR is virtually independent of metallicity. This is shown in Figure 10 for the case $\log (P/k) = 8.0$ cm^{-3} K. For clarity, only the SEDs for the 20 and 77.8 $M_\odot$ cases are shown here. The main difference is at shorter wavelengths, where the effect of the different absorption produced by the fixed column density ($\log N_{\rm H\,I} \sim 22.0$) can be clearly seen. At very long wavelengths, the continuum is dominated by the free-free emission, and the differences arise from the differences in the

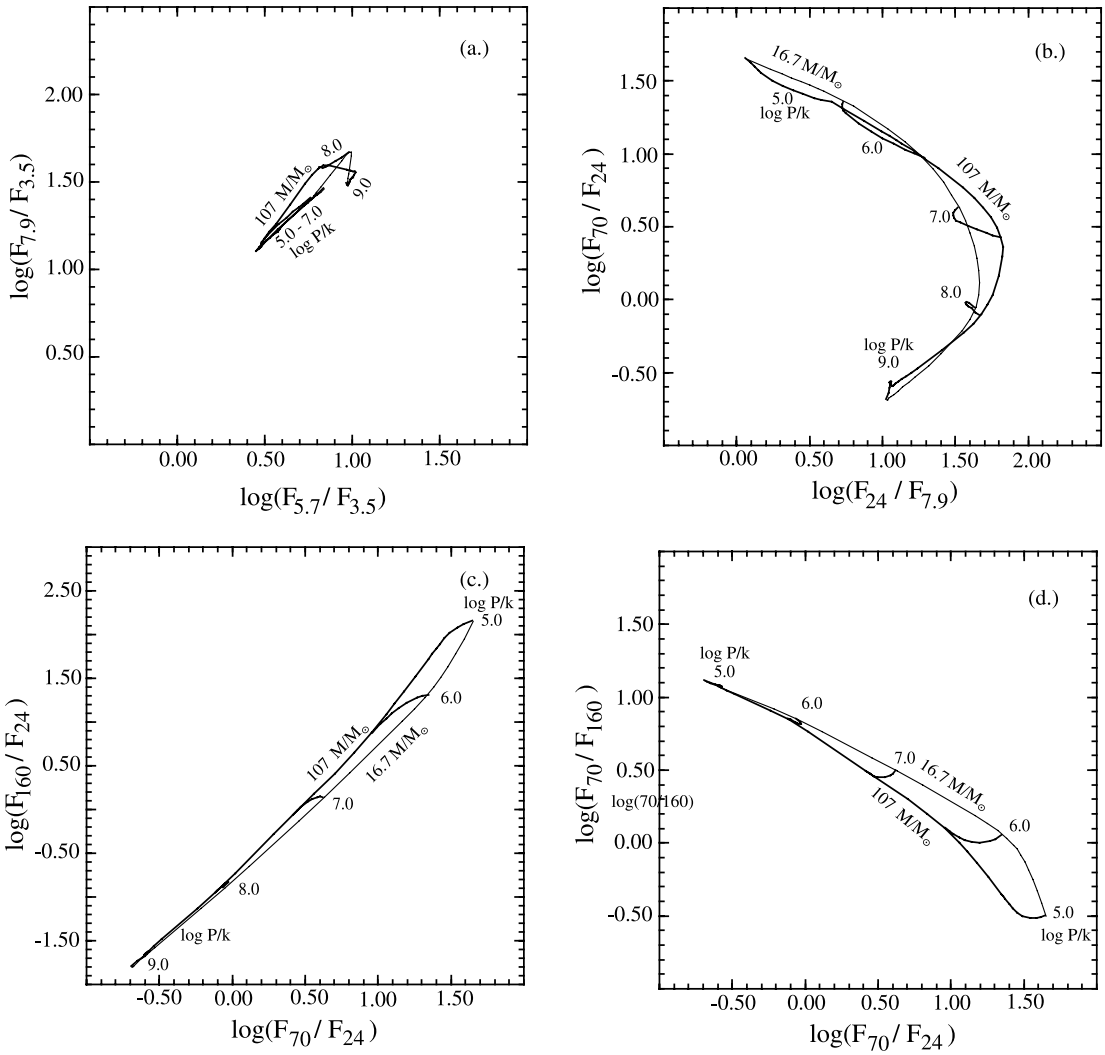

FIG. 11.—Theoretical *Spitzer* color-color diagrams for both the IRAC (*a*) and MIPS instruments (*remaining three panels*). These color-color diagrams are sensitive to the distribution of dust grain temperatures, and hence to the geometry of the dust with respect to the central source, and are not very sensitive to stellar mass. However, the large sensitivity to pressure should make this variable easy to measure with the MIPS instrument. The same is not true for the IRAC color-color diagrams; see (*a*), because the PAH emission (at low pressures) cannot be distinguished from the hot dust emission (at high pressures).

absorption of the ionizing photons by the dust within the H II region, which makes the ionized mass a function of the metallicity.

Unfortunately, the calibration problems of the *ISO* data prevent us from making a detailed comparison of the observations with our theoretical models. In particular, we cannot test whether the PAH features are weaker in those objects with hotter dust, since as longer wavelengths are observed, the resolution of the instruments decreases, and so the instrumental beam of *ISO* integrates over more, and presumably, cooler dust.

The position of the peak in the far-IR dust emission should be strongly correlated with pressure in the H II region. In general, we can say that most of the H II regions observed by Peeters et al. (2002) have the peak in their SED between 20 and 60 μm. This loosely confines the pressures variable within the range from $P/k = 10^6$ to 10^9 cm^{-3} K, agreeing with the pressures inferred from the position of these objects on Figures 2 and 3.

7. IR COLOR-COLOR DIAGRAMS

The theoretical SEDs presented in the previous section were passed through the transmission functions of the MIPS (Rieke et al. 2004) and IRAC (Fazio et al. 2004) instruments on the *Spitzer Space Telescope* (Werner et al. 2004) to produce theoretical color-color diagrams. Some of the more useful ones among these are presented in Figure 11.

In the case of the MIPS color-color diagrams, the theoretical colors vary over a very wide range because of the wide range in the dust temperature distributions in these models. Because this temperature distribution depends on $L_*/\langle r_{\rm neb}\rangle^2$, it is mostly degenerate in terms of the stellar luminosity L_* and the pressure, which determines (for a given stellar luminosity) the mean nebular radius $\langle r_{\rm neb}\rangle$. However, the range of colors covered by changing pressure is much greater than the change covered by changing stellar effective temperature at a given pressure. Therefore, these diagrams can be used as pressure diagnostics, even if the stellar effective temperature is only poorly known.

These MIPS color-color diagrams are effectively independent of the attenuation depth in the molecular shell surrounding the H II region, but we can expect that the thermal reemission from this shell will affect the SED and hence the color-color diagrams. Since the dust in such a shell will be much cooler than that of the H II region, we can expect a large additional flux in the 160 μm wave band and a lesser contribution to the MIPS

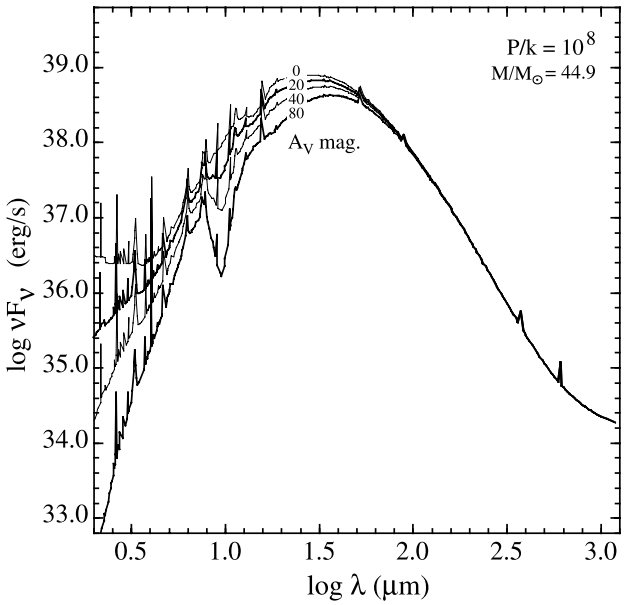

FIG. 12.—SED for a stellar mass of 44.9 $M_\odot$ and for fixed pressure, $P/k = 10^8$ cm^{-3} K, shown reddened by foreground extinctions of $A_V = 0$, 20, 40, and 80 mag.

70 μm wave band. The effect of this radiative transfer through the overlaying molecular cloud will be the subject of a future paper.

The color-color diagrams involving the IRAC wave bands are not very useful, since, as can be seen from Figure 6, the PAH features contribute strongly to these wave bands at low pressures, whereas the hot dust contributes strongly at high pressures. This makes the color-color diagrams degenerate in both mass and pressure for all except the highest pressure models. Furthermore, these wave bands are strongly affected by extinction by the overlying molecular shell, as can be seen in the example SED given in Figure 12 in the Appendix to this paper.

Apart from the IRAC $\log(F_{5.7}/F_{3.5})$ versus $\log(F_{7.9}/F_{3.5})$ color-color diagram shown in Figure 11, we have also computed color-color diagrams using the remaining *IRAC* wave bands. These are not shown here, but they also suffer the same problems as the one shown here.

8. CONCLUSIONS

In this paper we have presented both stellar mass and H II region diagnostics based on dusty, radiation-pressure-dominated photoionization models for compact and ultracompact H II regions, based on the TLUSTY model stellar atmospheres.

Despite the fact that the TLUSTY models are not fully self-consistent, being based on nondynamical stellar atmospheres, these models are remarkably successful in fitting a number of observational constraints. In particular, they successfully reproduce the observed relationship between the density and the thickness of the ionized layer, are consistent with the radio continuum luminosities of UC H II regions, and also provide a good description of observed excitation diagnostic plots involving ratios of infrared emission lines.

The question of what lies within UC H II regions can be fairly tightly constrained by these models, modulo the uncertainties produced by the atmospheric models adopted. The stellar mass (or effective temperature) can be inferred from the radio continuum flux (provided that the UC H II region is excited by a single star) or by the nebular excitation based on the [Ne III] 15.5 μm/[Ne II] 12.8 μm ratio versus either the [S IV] 10.5 μm/[Ar III] 9.8 μm or the [Ne III] 15.5 μm/[S III] 18.7 μm ratio. These diagnostics do not depend strongly on the metallicity of the gas in the H II region, and all of these lines are readily accessible with the *Spitzer* IRS instrument.

In addition, the extinction of the overlying shell of cool dusty gas can be constrained by observations of the [S IV]10.5 μm/[S III] 18.7 μm ratio, once the effective temperature or mass of the central star or stars has been determined using the other ratios. We find that the mean extinction to observed compact H II regions is about $A_V \sim 30$ mag.

The pressure in the ionized gas around the exciting stars can be determined in a number of ways. It can, of course, be directly inferred from an estimate of the mean electron density, $\langle n_e \rangle$, obtained from radio observations, or it can be estimated using either direct observations of the far-IR SED or *Spitzer* observations using the MIPS instrument. The models presented here provide a calibration of all of these observed quantities as a function of pressure. However, the transformation is not trivial because the absorption of the radiation field determines the pressure gradient through the H II region, leading to a strong radial density gradient. This gradient is a function of the metallicity as well as the pressure, and an appreciable fraction of both the ionizing photons and of the softer nonionizing UV photons may be absorbed in UC H II regions.

In all models for which the radiation pressure exceeds the gas pressure at the inner boundary of the H II region, the ionized plasma is essentially confined to a thin shell. Because of the effects of absorption of ionizing photons in our models, the Strömgren column is rather insensitive to the physical parameters and is consistent with the results by Churchwell (2002), who showed he Strömgren columns are consistent with $\log N_{\rm H\,II} \sim 21.5$ in most UC H II regions. In addition, if the radio observations are preferentially picking up on the high emission measure regions in the most compact UC H II regions, and therefore measuring the thickness of the ionized shell rather than the overall physical size of the H II region, then the observed density-diameter relationship can also be explained.

Finally, we find that the electron temperature of the model H II regions is found to depend on the chemical abundances, the pressure, and the effective temperature of the exciting star. We use our models to explicitly solve for each of these variables and so to rederive the slope of the Galactic abundance gradient. We find that $d\log({\rm O/H})/dR_G = 0.06 \pm 0.01$ dex kpc^{-1}. This brings the Galactic abundance gradient derived from compact H II regions into closer agreement with other techniques.

We wish to thank the referee, Claude Morisset, whose helpful comments led us to a major revision of the paper as originally submitted. We believe that the paper is much improved as a result. M. Dopita acknowledges the support of both the Australian National University and of the Australian Research Council (ARC) through his ARC Australian Federation Fellowship. M. A. D., R. S. S., and J. F. recognize the financial support of the ARC through Discovery Project grant DP0208445. O. C. acknowledges visiting student support under M. A. D.'s Federation Fellowship grant. L. J. K. acknowledges the receipt of a Hubble Fellowship.

APPENDIX

In the electronic version of this paper, we present the theoretical extinction curve by J. Fischera (2006, in preparation) for the solar vicinity based on a best fit to the absorption, emission, and elemental depletions. This has been sampled in exactly the same way as our theoretical SEDs to allow these to be reddened as desired to fit the observations. A short extract is given in Table A1 (below) to illustrate the format and content. In Table A2, the computed SEDs at solar metallicity are given in a machine-readable form for each value of the pressure at the ionization front ($\log P/k = 5.0$, 6.0, 7.0, 8.0, and 9.0 cm^{-3} K). A short extract is given below to illustrate the format and content for $\log P/k = 5.0$ cm^{-3} K.

Figure 12 is presented an example of the application of external extinction to one of the theoretical SEDs we have computed.

TABLE A1

THEORETICAL FOREGROUND EXTINCTION CURVE SAMPLED IN THE SAME BINS AS OUR MODEL SEDS

ν (Hz)	λ (μm)	A_λ/A_V
3.68697E+08	813112.104	1.7068E−11
4.03155E+08	743615.546	2.0407E−11
4.40833E+08	680058.734	2.4399E−11
4.82032E+08	621934.127	2.9173E−11
5.27082E+08	568777.534	3.4881E−11
5.76342E+08	520164.160	4.1705E−11
6.30206E+08	475705.706	4.9865E−11
6.89103E+08	435047.237	5.9621E−11
7.53505E+08	397863.744	7.1286E−11

NOTE.—Table A1 is published in its entirety in the electronic edition of the *Astrophysical Journal*. A portion is shown here for guidance regarding its form and content.

TABLE A2

COMPACT H II REGION SEDS (νF_ν) FOR SOLAR METALLICITY AND $\log P/k = 5.0$ cm^{-3} K

		$\nu F\nu$ (ergs s^{-1})								
ν (Hz)	λ (μm)	16.7 $M_\odot$	20.0 $M_\odot$	24 $M_\odot$	30 $M_\odot$	36 $M_\odot$	45 $M_\odot$	56 $M_\odot$	78 $M_\odot$	106.9 $M_\odot$
3.687E+08	813112	4.753E+31	1.011E+32	2.266E+32	3.472E+32	4.635E+32	6.179E+32	1.021E+33	1.329E+33	1.363E+33
4.031E+08	743615	3.600E+32	6.249E+32	1.209E+33	1.704E+33	2.035E+33	2.429E+33	3.773E+33	4.420E+33	5.573E+34
4.408E+08	680058	2.203E+39	2.915E+39	4.618E+39	5.605E+39	6.049E+39	6.689E+39	9.497E+39	1.016E+40	1.003E+40
4.820E+08	621934	6.078E+31	1.292E+32	2.896E+32	4.437E+32	5.922E+32	7.895E+32	1.305E+33	1.699E+33	1.741E+33

NOTE.—Table A2 is published in its entirety in the electronic edition of the *Astrophysical Journal*. A portion is shown here for guidance regarding its form and content.

REFERENCES

Afflerbach, A., Churchwell, E., Acord, J. M., Hofner, P., Kurtz, S., & DePree, C. G. 1996, ApJS, 106, 423
Afflerbach, A., Churchwell, E., & Werner, M. W. 1997, ApJ, 478, 190
Allende Prieto, C., Lambert, D. L., & Asplund, M. 2001, ApJ, 556, L63
———. 2002, ApJ, 573, L137
Arthur, S. J., Kurtz, S. E., Franco, J., & Albarrán, M. Y. 2004, ApJ, 608, 282
Asplund, M. 2000, A&A, 359, 755
Asplund, M., Nordlund, A., Trampedach, R., & Stein, R. F. 2000, A&A, 359, 743
Bottorff, M., LaMothe, J., Momjian, E., Verner, E., Vinković, D., & Ferland, G. 1998, PASP, 110, 1040
Burton, M. G., et al. 2000, ApJ, 542, 359
Charbonnel, C., Meynet, G., Maeder, A., Schaller, G., & Schaerer, D. 1993, A&AS, 101, 415
Christiansen, J. 2003, honors thesis, Australian Natl. Univ.
Churchwell, E. 2002, ARA&A, 40, 27
Churchwell, E., et al. 2004, ApJS, 154, 322
Crowther, P. A., et al. 1999, A&A, 350, 1007
Dopita, M. A., Groves, B. A., Sutherland, R. S., & Kewley, L. J. 2003, ApJ, 583, 727
Dopita, M. A., & Sutherland, R. S. 2003, Astrophysics of the Diffuse Universe (Berlin: Springer)
Dopita, M. A., Sutherland, R. S., Groves, B. A., & Binette, L. 2002, ApJ, 572, 753
Dopita, M. A., et al. 2005, ApJ, 619, 755
Fazio, G. G., et al. 2004, ApJS, 154, 39
Garay, G., & Lizano, S. 1999, PASP, 111, 1049
Grevesse, N., & Sauval, A. J. 1998, Space Sci. Rev., 85, 161
Groves, B. A., Dopita, M. A., & Sutherland, R. S. 2004a, ApJS, 153, 9
———. 2004b, ApJS, 153, 75
Hillier, D. J., & Miller, D. L. 1998, ApJ, 496, 407
Houck, J. R., et al. 2004, ApJS, 154, 18
Inoue, A. K. 2001, AJ, 122, 1788
Inoue, A. K., Hirashita, H., & Kamaya, H. 2000, PASJ, 52, 539
———. 2001, ApJ, 555, 613
Jenkins, E. B., Jura, M., & Loewenstein, M. 1983, ApJ, 270, 88
Kewley, L. J., Dopita, M. A., Sutherland, R. S., Heisler, C. A., & Trevena, J. 2001, ApJ, 556, 121
Kim, K., & Koo, B. 2001, ApJ, 549, 979
Kimura, H., Mann, I., & Jessberger, E. K. 2003, ApJ, 582, 846
Kurtz, S., Churchwell, E., & Wood, D. O. S. 1994, ApJS, 91, 659

Kurucz, R. 1991, in Stellar Atmospheres: Beyond Classical Models, ed. L. Crivellari, I. Hubeny, & D. Hummer (NATO ASI Ser. C., 341; Dordrecht: Kluwer), 441
———. 1994, CD-ROM No. 19, Solar Abundance Model Atmospheres for 0, 1, 2, 4 and 8 km/s (Cambridge: Smithsonian Astrophys. Obs.), 19
Lanz, T., & Hubeny, I. 2003, ApJS, 146, 417 (erratum 147, 225)
Lumsden, S. L., Puxley, P. J., Hoare, M. G., & Ridge, N. A. 2003, MNRAS, 340, 799
Maeder, A., & Meynet, G. 1988, A&AS, 76, 411
———. 1989, A&A, 210, 155
———. 1994, A&A, 287, 803
Martín-Hernández, N. L., van der Hulst, J. M., & Tielens, A. G. G. M. 2003, A&A, 407, 957
Martín-Hernández, N. L., et al. 2002, A&A, 381, 606
Mendoza, C. 1983, in IAU Symp. 103, Planetary Nebuale, ed. D. R. Flower (Dordrecht: Reidel), 143
Mezger, P. G., Smith, L. F., & Churchwell, E. 1974, A&A, 32, 269
Morisset, C. 2004, ApJ, 601, 858
Morisset, C., Schaerer, D., Bouret, J.-C., & Martins, F. 2004, A&A, 415, 577
Naqvi, A. M. 1951, Ph.D. thesis, Harvard Univ.
Natta, A., & Panagia, N. 1976, A&A, 50, 191
Oey, M. S., Dopita, M. A., Shields, J. C., & Smith, R. C. 2000, ApJS, 128, 511
Panagia, N. 1974, ApJ, 192, 221
Pauldrach A. W. A., Hoffmann, T. L., & Lennon, M. 2001, A&A, 375, 161
Peeters, E., et al. 2002, A&A, 381, 571
Petrosian, V., Silk, J., & Field, G. B. 1972, ApJ, 177, L69
Rieke, G. H., et al. 2004, ApJS, 154, 25
Rigby, J. R., & Rieke, G. H. 2004, ApJ, 606, 237
Sarazin, C. L. 1977, ApJ, 211, 772
Savage, B. D., & Sembach, K. R. 1996, ARA&A, 34, 279
Schaerer, D., Charbonnel, C., Meynet, G., Maeder, A., & Schaller, G. 1993a, A&AS, 102, 339
Schaerer, D., & de Koter, A. 1997, A&A, 322, 598
Schaerer, D., Meynet, G., Maeder, A., & Schaller, G. 1993b, A&AS, 98, 523
Schaller, G., Schaerer, D., Meynet, G., & Maeder, A. 1992, A&AS, 96, 269
Shaver, P. A., McGee, R. X., Newton, L. N., Danks, A. C., & Pottasch, S. R. 1983, MNRAS, 204, 53
Shields, J. C., & Kennicutt, R. C. 1995, ApJ, 454, 807
Simpson, J. P., et al. 1995, ApJ, 444, 721
Smartt, S. J., & Rolleston, W. R. J. 1997, ApJ, 481, L47
Smith, L. F., Biermann, P., & Mezger, P. G. 1978, A&A, 66, 65
Smith, L. J., Norris, R. P. F., & Crowther, P. A. 2002, MNRAS, 337, 1309
Walmsley, C. M. 1995, Rev. Mex. AA, Ser. Conf., 1, 137
Werner, M. W., et al. 2004, ApJS, 154, 1
Whitney, B. A., et al. 2004, ApJS, 154, 315
Wood, D. O. S., & Churchwell, E. 1989, ApJS, 69, 831